

Potentials of Mean Force and Permeabilities for Carbon Dioxide, Ammonia, and Water Flux across a Rhesus Protein Channel and Lipid Membranes

Jochen S. Hub,^{*,†} Fritz K. Winkler,[‡] Mike Merrick,[§] and Bert L. de Groot^{||}

Department of Cell and Molecular Biology, Uppsala University, Box 596, 75124 Uppsala, Sweden, Biomolecular Research, Paul Scherrer Institut, CH-5232 Villigen, Switzerland, The Department of Molecular Microbiology, John Innes Centre, Colney Lane, Norwich, Norfolk NR4 7UH, U.K., and Computational Biomolecular Dynamics Group, Max-Planck-Institute for Biophysical Chemistry, Am Fassberg 11, 37077 Göttingen, Germany

Received March 12, 2010; E-mail: jochen@xray.bmc.uu.se

Abstract: As a member of the ubiquitous ammonium transporter/methylamine permease/Rhesus (Amt/MEP/Rh) family of membrane protein channels, the 50 kDa Rhesus channel (Rh50) has been implicated in ammonia (NH₃) and, more recently, also in carbon dioxide (CO₂) transport. Here we present molecular dynamics simulations of spontaneous full permeation events of ammonia and carbon dioxide across Rh50 from *Nitrosomonas europaea*. The simulations show that Rh50 is functional in its crystallographic conformation, without the requirement for a major conformational change or the action of a protein partner. To assess the physiological relevance of NH₃ and CO₂ permeation across Rh50, we have computed potentials of mean force (PMFs) and permeabilities for NH₃ and CO₂ flux across Rh50 and compare them to permeation through a wide range of lipid membranes, either composed of pure lipids or composed of lipids plus an increasing cholesterol content. According to the PMFs, Rh50 is expected to enhance NH₃ flux across dense membranes, such as membranes with a substantial cholesterol content. Although cholesterol reduces the intrinsic CO₂ permeability of lipid membranes, the CO₂ permeabilities of all membranes studied here are too high to allow significant Rh50-mediated CO₂ flux. The increased barrier in the PMF for water permeation across Rh50 shows that Rh50 discriminates 40-fold between water and NH₃. Thus, Rh50 channels complement aquaporins, allowing the cell to regulate water and NH₃ flux independently. The PMFs for methylamine and NH₃ are virtually identical, suggesting that methylamine provides an excellent model for NH₃ in functional experiments.

Introduction

The integral membrane proteins of the Rhesus (Rh) family are present in all animals including humans and are very occasionally found in prokaryotes.¹ They were originally identified as mammalian blood group antigens expressed on red blood cells, but their function remained unclear until it was recognized that they share homology with the ammonium transport (Amt) proteins.^{2,3} The latter are present in nearly all bacteria, archaea, fungi and plants and play an important role in the nutritional uptake of ammonium under conditions of nitrogen limitation. In humans, the Rh antigens are carried by two erythrocyte cell membrane proteins, RhD and RhCE (also termed Rh30; apparent molecular mass 30 kDa).⁴ Rh30 proteins are now thought to be functionally inactive variants of the

homologous Rh50 (50 kDa) glycoproteins. In mammals, three Rh50 family members have been identified so far. RhAG (originally Rh-associated glycoprotein) is expressed in erythrocytes, while RhBG and RhCG are expressed in various epithelial tissues. Both RhAG and RhCG have been shown to play a role in transmembrane ammonium transport.^{5,6} However it has also been proposed that Rh50 proteins facilitate carbon dioxide (CO₂) transport, and indeed this has been speculated to be their genuine biological function.^{7–9} Furthermore experimental evidence for CO₂ transport by human Rh50 proteins has been reported for RhAG.¹⁰

Numerous functional studies using biochemical, electrophysiological and biological methods have been reported for representatives of both the Amt and Rh families, and high resolution

[†] Uppsala University.

[‡] Paul Scherrer Institut.

[§] John Innes Centre.

^{||} Max-Planck-Institute for Biophysical Chemistry.

(1) Huang, C.-H.; Peng, J. *Proc. Natl. Acad. Sci. U.S.A.* **2005**, *102*, 15512–15517.

(2) Marini, A. M.; Urrestarazu, A.; Beauwens, R.; André, B. *Trends Biochem. Sci.* **1997**, *22*, 460–461.

(3) Marini, A. M.; Matassi, G.; Raynal, V.; André, B.; Cartron, J. P.; Chérif-Zahar, B. *Nat. Genet.* **2000**, *26*, 341–344.

(4) Westhoff, C. M. *Transfusion* **2004**, *44*, 1663–1673.

(5) Biver, S.; Belge, H.; Bourgeois, S.; Vooren, P. V.; Nowik, M.; Scohy, S.; Houillier, P.; Szpirer, J.; Szpirer, C.; Wagner, C. A.; Devuyst, O.; Marini, A. M. *Nature* **2008**, *456*, 339–343.

(6) Ripoche, P.; Bertrand, O.; Gane, P.; Birkenmeier, C.; Colin, Y.; Cartron, J.-P. *Proc. Natl. Acad. Sci. U.S.A.* **2004**, *101*, 17222–17227.

(7) Kustu, S.; Inwood, W. *Transfus. Clin. Biol.* **2006**, *13*, 103–110.

(8) Peng, J.; Huang, C. H. *Transfus. Clin. Biol.* **2006**, *13*, 85–94.

(9) Soupené, E.; Inwood, W.; Kustu, S. *Proc. Natl. Acad. Sci. U.S.A.* **2004**, *101*, 7787–7792.

(10) Endeward, V.; Cartron, J.-P.; Ripoche, P.; Gros, G. *FASEB J.* **2008**, *22*, 64–73.

X-ray structures are available for two bacterial Amt proteins,^{11–13} the bacterial Rh50 protein from *Nitrosomonas europaea* (NeRh50)^{14,15} and, as of very recently, for human RhCG.¹⁶

Despite these efforts, major functional issues have remained controversial. The first issue concerns the nature of the ammonium transport mechanism, that is, whether it is electrogenic or electroneutral. Presently, electroneutral transport of NH₃ is favored for Rh proteins and in particular for human Rh50 proteins.^{5,6,17,18} Electrogenic transport is favored for Amt proteins,^{19–21} but there may be exceptions.^{22,23} The second issue concerns the biological function of Rh proteins, that is, whether they facilitate NH₃ or CO₂ transport or both. A major difficulty in experiments to determine function, whether using *in vitro* or cellular assays, is that NH₃ and particularly CO₂ permeate lipid membranes relatively easily and their transport is quantified by indirect analytical means depending in the case of CO₂ on kinetic models.^{24,25} Moreover unstirred layers or incomplete mixing can cause problems in the interpretation of the experimental results.^{24–26} Bilayer permeabilities of H₂O and NH₃ are known to vary with lipid composition, typically within 1 order of magnitude.²⁷ With CO₂, this does not appear to be the case^{25,28} but unstirred layer effects may mask differences.²⁹ Very low NH₃ or CO₂ permeabilities have been reported for membranes of some specific tissues,^{30,31} and their origin is presently not understood. In summary, caution is required when molecular explanations are sought to rationalize reported permeabilities.

Structurally, the most conserved region of the homotrimeric Rh and Amt proteins is a narrow substrate-conduction pore through the middle of each monomer. The strongly hydrophobic

nature of this pore, which is conserved throughout the Amt/Rh family, appears to disfavor passage of ammonium ions, as opposed to ammonia, and suggests conservation of both substrate and transport mechanism. However, the vestibule at the extracytoplasmic end of the conduction pore has distinctive features in Amt and Rh proteins. Specifically, the residues that constitute a high affinity ammonium ion binding site at the base of this vestibule are conserved in Amt proteins but absent in Rh proteins.¹⁴ This appears rational because whereas Amt proteins are thought to function in scavenging ammonium at very low extracellular concentrations, Rh proteins are more likely to function in equilibrating ammonium across cell membranes.⁵

Molecular dynamics simulations offer an alternative approach to investigating the intrinsic substrate conduction properties of lipid bilayers and membrane channels.³² The functional determinants of AmtB from *E. coli* have been studied extensively by computational methods, mainly to clarify whether the electrogenic or electroneutral form of ammonium is transported by AmtB, with a focus on the binding mechanism of ammonium, and to identify the most likely deprotonation site of ammonium.^{33–40} The calculations showed that permeation of NH₄⁺ is highly disfavored versus the permeation of neutral NH₃. However, the deprotonation mechanism for NH₄⁺ remains controversial. Both the conserved Asp160^{34,35} and water molecules were suggested as proton acceptors,^{38,39} and a deprotonation mechanism via an intermediate hydroxyl ion has been proposed.³⁷ Likewise, the existence of a water chain in the pore of AmtB has been controversially discussed.^{34,38,41} So far, no computational studies on the Rh channels have been published.

Here we present the potentials of mean force of full permeation events of CO₂ and NH₃ across the Rh50 channel from *N. europaea* (NeRh50), and compare the results to the energetics of CO₂ and NH₃ permeation across a large set of different lipid membranes, containing either exclusively lipids or lipids plus an increasing cholesterol content. In addition, we have carried out extensive equilibrium simulations in which CO₂ and NH₃ were able to diffuse freely across NeRh50 and across the lipid membranes, allowing us to derive single-channel and membrane permeabilities. The simulations show that, due to the generally high intrinsic CO₂ permeability of lipid membranes, Rh50 is only expected to contribute to CO₂ flux in membranes with an exceptionally low intrinsic CO₂ permeability. In contrast, Rh50 enhances NH₃ flux across moderately dense membranes such as membranes with a high cholesterol content. The pore structure of the recently resolved human RhCG channel¹⁶ is highly similar to the pore of NeRh50,

- (11) Khademi, S.; O'Connell, J.; Remis, J.; Robles-Colmenares, Y.; Miercke, L. J. W.; Stroud, R. M. *Science* **2004**, *305*, 1587–1594.
- (12) Zheng, L.; Kostrewa, D.; Berneche, S.; Winkler, F. K.; Li, X.-D. *Proc. Natl. Acad. Sci. U.S.A.* **2004**, *101*, 17090–17095.
- (13) Andrade, S. L. A.; Dickmanns, A.; Ficner, R.; Einsle, O. *Proc. Natl. Acad. Sci. U.S.A.* **2005**, *102*, 14994–14999.
- (14) Lupo, D.; Li, X.-D.; Durand, A.; Tomizaki, T.; Cherif-Zahar, B.; Matassi, G.; Merrick, M.; Winkler, F. K. *Proc. Natl. Acad. Sci. U.S.A.* **2007**, *104*, 19303–19308.
- (15) Li, X.; Jayachandran, S.; Nguyen, H.-H. T.; Chan, M. K. *Proc. Natl. Acad. Sci. U.S.A.* **2007**, *104*, 19279–19284.
- (16) Gruswitz, F.; Chaudhary, S.; Ho, J. D.; Schlessinger, A.; Pezeshki, B.; Ho, C.-M.; Sali, A.; Westhoff, C. M.; Stroud, R. M. *Proc. Natl. Acad. Sci. U.S.A.* **2010**, *107*, 9638–9643.
- (17) Zidi-Yahiaoui, N.; Mouro-Chanteloup, I.; D'Ambrosio, A.-M.; Lopez, C.; Gane, P.; van Kim, C. L.; Cartron, J.-P.; Colin, Y.; Ripoche, P. *Biochem. J.* **2005**, *391*, 33–40.
- (18) Zidi-Yahiaoui, N.; Callebaut, I.; Genetet, S.; Kim, C. L. V.; Cartron, J.-P.; Colin, Y.; Ripoche, P.; Mouro-Chanteloup, I. *Am. J. Physiol.* **2009**, *297*, C537–C547.
- (19) Fong, R. N.; Kim, K.-S.; Yoshihara, C.; Inwood, W. B.; Kustu, S. *Proc. Natl. Acad. Sci. U.S.A.* **2007**, *104*, 18706–18711.
- (20) Javelle, A.; Lupo, D.; Ripoche, P.; Fulford, T.; Merrick, M.; Winkler, F. K. *Proc. Natl. Acad. Sci. U.S.A.* **2008**, *105*, 5040–5045.
- (21) Mayer, M.; Schaaf, G.; Mouro, I.; Lopez, C.; Colin, Y.; Neumann, P.; Cartron, J.-P.; Ludewig, U. *J. Gen. Physiol.* **2006**, *127*, 133–144.
- (22) Neuhäuser, B.; Dynowski, M.; Ludewig, U. *FEBS Lett.* **2009**, *583*, 2833–2838.
- (23) Walter, B.; Küspert, M.; Ansorge, D.; Krämer, R.; Burkovski, A. *J. Bacteriol.* **2008**, *190*, 2611–2614.
- (24) Endeward, V.; Gros, G. *J. Physiol.* **2009**, *587*, 1153–1167.
- (25) Missner, A.; Kügler, P.; Saparov, S. M.; Sommer, K.; Mathai, J. C.; Zeidel, M. L.; Pohl, P. *J. Biol. Chem.* **2008**, *283*, 25340–25347.
- (26) Missner, A.; Pohl, P. *ChemPhysChem* **2009**, *10*, 1405–1414.
- (27) Lande, M. B.; Donovan, J. M.; Zeidel, M. L. *J. Gen. Physiol.* **1995**, *106*, 67–84.
- (28) Prasad, G. V. R.; Coury, L. A.; Finn, F.; Zeidel, M. L. *J. Biol. Chem.* **1998**, *273*, 33123–33126.
- (29) Hub, J. S.; de Groot, B. L. *Biophys. J.* **2006**, *91*, 842–848.
- (30) Kikeri, D.; Sun, A.; Zeidel, M. L.; Hebert, S. C. *Nature* **1989**, *339*, 478–480.
- (31) Waisbren, S. J.; Geibel, J. P.; Modlin, I. M.; Boron, W. F. *Nature* **1994**, *368*, 332–335.

- (32) Hub, J. S.; de Groot, B. L. *Proc. Natl. Acad. Sci. U.S.A.* **2008**, *105*, 1198–1203.
- (33) Luzhkov, V. B.; Almlöf, M.; Nervall, M.; Åqvist, J. *Biochemistry* **2006**, *45*, 10807–10814.
- (34) Nygaard, T. P.; Rovira, C.; Peters, G. H.; Jensen, M. Ø. *Biophys. J.* **2006**, *91*, 4401–4412.
- (35) Lin, Y.; Cao, Z.; Mo, Y. *J. Am. Chem. Soc.* **2006**, *128*, 10876–10884.
- (36) Yang, H.; Xu, Y.; Zhu, W.; Chen, K.; Jiang, H. *Biophys. J.* **2007**, *92*, 877–885.
- (37) Cao, Z.; Mo, Y.; Thiel, W. *Angew. Chem., Int. Ed.* **2007**, *46*, 6811–6815.
- (38) Bostick, D. L.; Brooks, C. L. *PLoS Comput. Biol.* **2007**, *3*, e22.
- (39) Bostick, D. L.; Brooks, C. L. *Biophys. J.* **2007**, *92*, L103–L105.
- (40) Ishikita, H.; Knapp, E.-W. *J. Am. Chem. Soc.* **2007**, *129*, 1210–1215.
- (41) Lamoureux, G.; Klein, M. L.; Berneche, S. *Biophys. J.* **2007**, *92*, L82–L84.

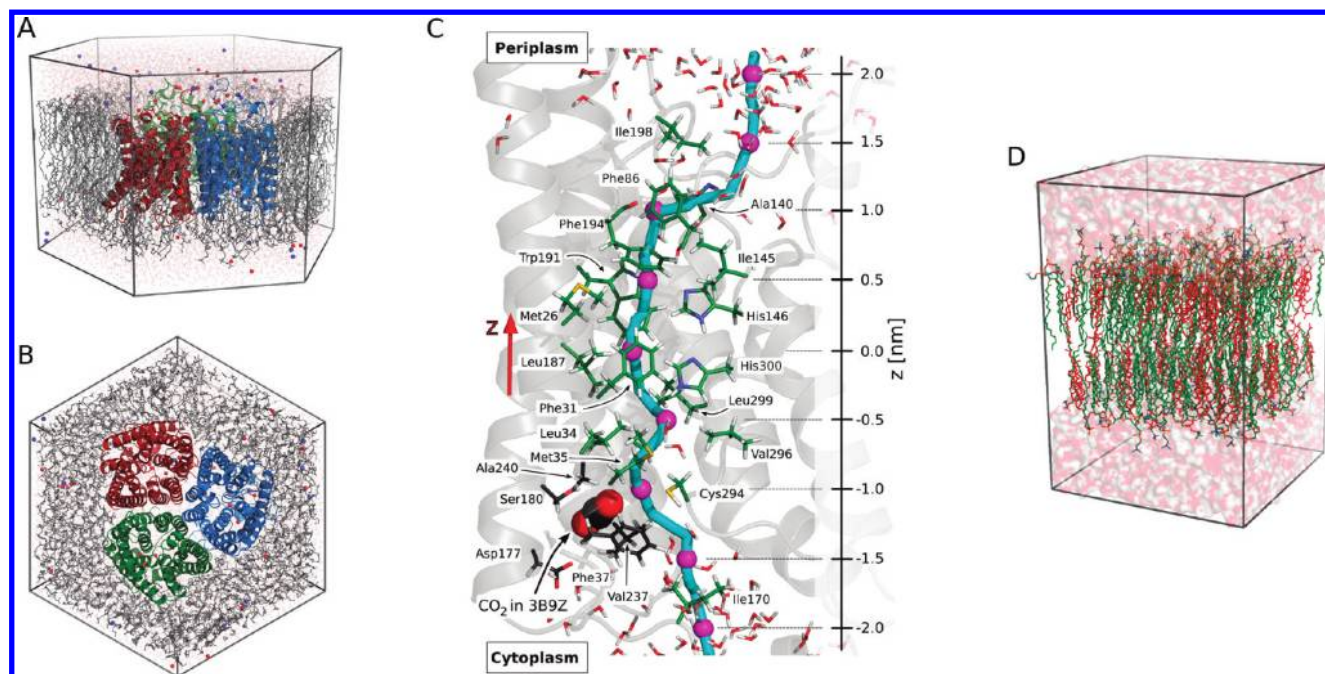


Figure 1. A typical simulation system of an NeRh50 trimer in side view (A) and top view (B). The protein is shown in colored cartoon representation, lipids are shown in gray, and sodium and chloride ions are shown as red and blue spheres, respectively. (C) Simulation snapshot of the NeRh50 channel. Some pore-aligning residues and water molecules are shown in stick representation. The course of the pore as derived by HOLE²⁷ is represented by a cyan tube. To facilitate the interpretation of the NeRh50 PMFs (Figures 2A and 4A), the z -coordinate is indicated by magenta spheres, with one sphere per 0.5 nm (compare z axis at the right). A CO₂ molecule near the CO₂ position in the 3B9Z structure¹⁵ is shown in sphere representation, and the residues forming the respective binding pocket as black sticks. (D) A typical simulation box of a lipid membrane containing 40 mol % of cholesterol. Carbon atoms of lipids are shown in green and carbon atoms of cholesterol in red. Water is shown as a transparent surface.

suggesting that the results here derived for a bacterial Rh50 hold qualitatively for human Rh50 channels as well.

Results

CO₂ Potentials of Mean Force. Figure 2A presents the potential of mean force (PMF) for CO₂ permeation across NeRh50 as a black curve and the respective 67% confidence intervals as gray areas. The z -coordinate along the pore is visualized in Figure 1C. Surprisingly, the main barrier of 14.5 kJ/mol is not located at the pore-occluding phenyl ring of Phe194 ($z \approx 0.65$ nm), but at the backbone carbonyl oxygen of Phe194 (Phe194-O, $z \approx 1.0$ nm). Visual inspection of the simulation trajectories showed that, in the absence of CO₂, this oxygen atom forms a stable hydrogen bond to a nearby water molecule, located either at the position of crystal water HOH482 of the 3B9W structure or at a position 1.5 Å displaced toward the channel entrance. Upon passage of CO₂, the water–Phe194-O H-bond is partially lost, presumably inducing the barrier in the PMF. This phenomenon is quantified in Figure 3, which plots the average energy of the water–Phe194-O H-bond as a function of CO₂ position. Remarkably, the H-bond is weakened by approximately 20 kJ/mol upon passage of CO₂. Hence, an indirect, water-mediated effect accounts for the main barrier in the PMF. The related analysis for the nearby carbonyl oxygen of Ala140 showed that a frequent H-bond between water and Ala140 is much less affected by the permeating CO₂ (not shown). During the permeation event, the channel did not undergo any conformational change, suggesting that small thermal fluctuations of the phenyl ring of Phe194 are sufficient to allow the passage of small solutes. The position of the CO₂ molecule in the NeRh50 X-ray structure resolved by Li et al.

(PDB code 3B9Z)¹⁵ is indicated by a red arrow in Figure 2A, close to the local minimum at $z = -1$ nm (compare Figure 1C).

CO₂ permeation across NeRh50 is only expected to contribute substantially to the total CO₂ flux if the barrier across NeRh50 is substantially lower than the barrier for CO₂ permeation across the surrounding lipid membrane. Here we consider CO₂ permeation across nine model membranes, with four membranes containing exclusively lipids and five membranes containing lipids plus an increasing cholesterol content. The pure lipid membranes are characterized by an increasing area per lipid and, hence, decreasing densities of the aliphatic tails. (1) A membrane of pure POPE (palmitoyloleoylphosphatidylethanolamine), (2) composed of a 3:1 mixture of POPE and POPG (palmitoyloleoylphosphatidylglycerol), (3) composed of an equal mixture of POPE and POPC (palmitoyloleoylphosphatidylcholine), and (4) of pure POPC. These four model membranes will in the following be referred to as PE, PE/PG, PE/PC, and PC membranes, respectively. The compositions of the two leaflets were identical in all membranes. Phosphatidylethanolamine (PE) lipids, in particular POPE, are abundant in bacterial membranes, typically in an approximately 3:1 mixture with phosphatidylglycerol (PG) lipids. Animal membranes such as the red blood cell membrane contain large amounts of both PE and phosphatidylcholine (PC) lipids.

Figure 2B displays the PMFs for CO₂ permeation across the PE membrane (black curve), the PC membrane (red curve), the PE/PC membrane (green curve), and the PE/PG membrane (magenta curve). For the membranes containing only PE and PC lipids, the main barriers at the lipid head groups are smaller than 6 kJ/mol, indicating that these membranes are highly permeable to CO₂. The PG head groups in the PE/PG membrane

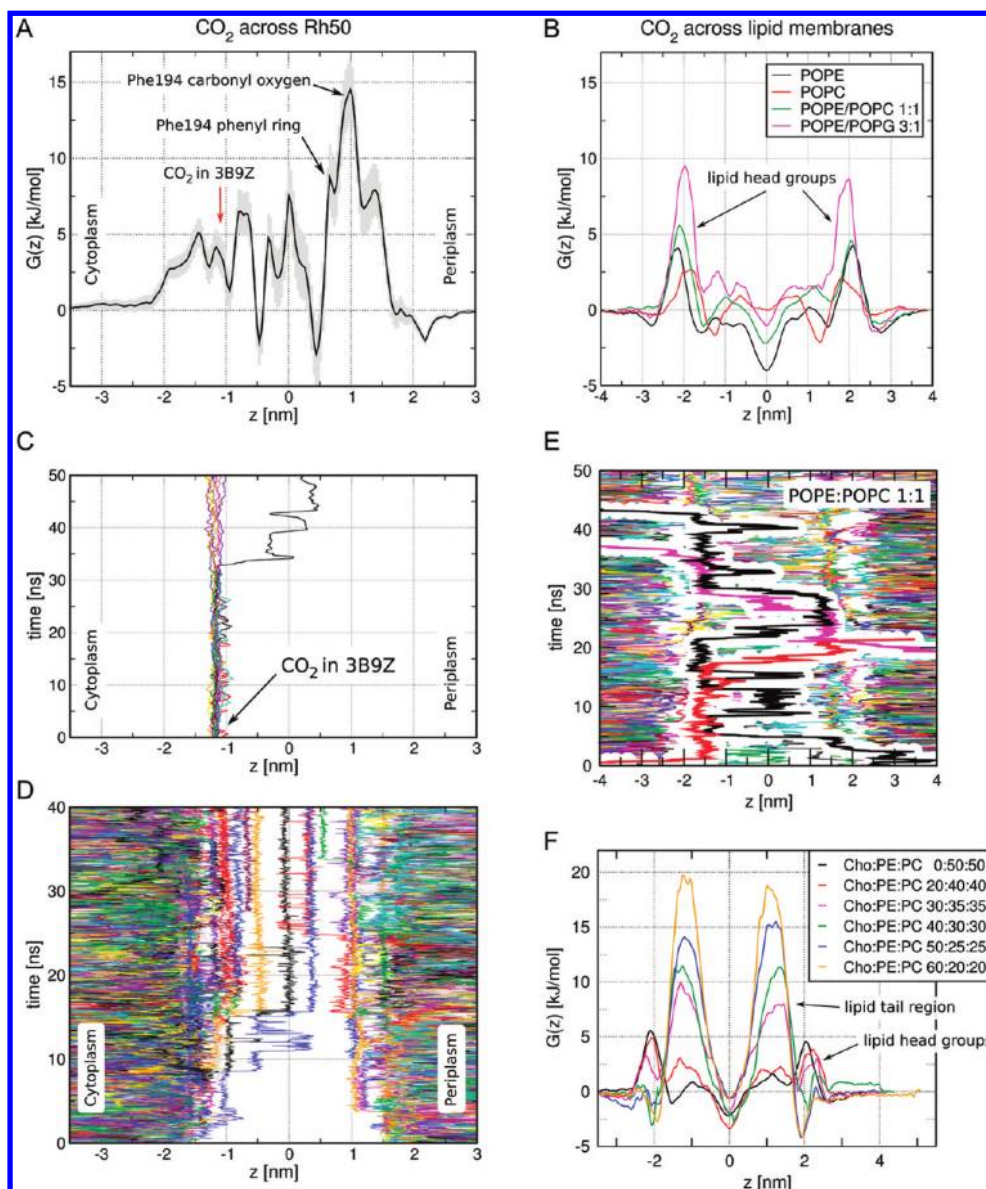


Figure 2. CO₂ permeation across the NeRh50 channel and lipid membranes. (A) Potential of mean force (PMF) for CO₂ permeation across NeRh50. The statistical uncertainty (67% confidence interval) is indicated by a gray area around the PMF. (B) PMFs for CO₂ permeation through lipid membranes composed of pure POPE (black), pure POPC (red), an equal mixture of POPE and POPC (green), and of a 3:1 mixture of POPE and POPG (magenta). (C) Trajectories of free (unrestrained) CO₂ molecules starting at the CO₂ position of the 3B9Z X-ray structure, and (D) starting at different positions in the bulk water. (E) Trajectories of free CO₂ molecules permeating across the lipid membrane composed of POPE and POPC (green PMF in B). Three full permeation events are highlighted as thick black, red and magenta lines. For visualization, all trajectory curves were slightly smoothed by running averages. (F) Influence of cholesterol on the CO₂ permeability of lipid membranes. Potentials of mean force (PMFs) of CO₂ permeation across membranes containing an equal mixture of POPE and POPC plus and increasing cholesterol content of 0, 20, 30, 40, 50, and 60 mol %.

induce an increased barrier of 9 kJ/mol. The statistical uncertainties at the main barriers for the PE, PC, and PE/PC membranes are ~ 1 kJ/mol, and ~ 2 kJ/mol for the PE/PG membrane. By comparison to Figure 2A, the main barrier for CO₂ permeation across the NeRh50 channel is at least ≈ 5 kJ/mol higher than the barrier for CO₂ permeation across the lipid membranes, suggesting that Rh50 does not contribute to CO₂ flux across such membranes.

Sterols are known to modulate the permeability of lipid membranes. Animal membranes frequently contain cholesterol, which reduces water⁴² and O₂⁴³ permeability, whereas hopanoids, the surrogate for sterols in bacteria, play a role in modulating the permeability of bacterial membranes.⁴⁴ The genome of *N. europaea* encodes a squalene-hopene synthase

gene, suggesting that NeRh50 may be expressed in membranes containing hopanoids. To assess if NeRh50 could act as a relevant CO₂ channel in membranes with substantial sterol or hopanoid content, we have computed the PMFs for CO₂ permeation across membranes with an equal mixture of POPE and POPC plus an increasing cholesterol content of 20, 30, 40, 50, and 60 mol %. As shown in Figure 2F, cholesterol induces an increased barrier against CO₂ translocation given a cholesterol

(42) Mathai, J. C.; Tristram-Nagle, S.; Nagle, J. F.; Zeidel, M. L. *J. Gen. Physiol.* **2008**, *131*, 69–76.

(43) Subczynski, W. K.; Hyde, J. S.; Kusumi, A. *Proc. Natl. Acad. Sci. U.S.A.* **1989**, *86*, 4474–4478.

(44) Welander, P. V.; Hunter, R. C.; Zhang, L.; Sessions, A. L.; Summons, R. E.; Newman, D. K. *J. Bacteriol.* **2009**, *191*, 6145–6156.

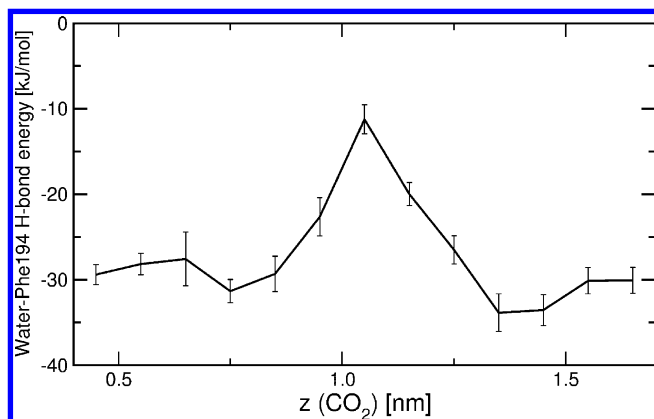


Figure 3. Energy of the hydrogen bond between water and the carbonyl oxygen of Phe194, as a function of CO₂ position. Upon passage of CO₂, the water–Phe194 hydrogen bond is partially lost, presumably inducing the main barrier in the PMF (compare Figure 2A).

concentration of ≥ 30 mol %. The statistical uncertainties of the PMFs for cholesterol-containing membranes are ~ 2 kJ/mol. For RBCs with a cholesterol concentration between 40 and 50 mol %, for instance, the PMFs suggest a barrier of ~ 13 kJ/mol (green and blue curves in Figure 2F). However, assuming a NeRh50 expression density similar to the RhAG density in RBCs,⁶ such barriers are still too low to render NeRh50 a physiological CO₂ channel (see Discussion). Any role of NeRh50 as a CO₂ channel is therefore unlikely in membranes composed of mainly POPE, POPC, and cholesterol.

CO₂ Permeation across NeRh50 and Lipid Membranes. We have complemented the PMFs by extensive simulations in which CO₂ was allowed to diffuse freely across the NeRh50 channel or across lipid membranes. These simulations allow one to estimate directly single-channel and membrane permeabilities and, consequently, validate whether the main barrier together with a rate ansatz can account for differences in solute permeability. Accordingly, we assumed the permeabilities P_s for a solute s to be proportional to

$$P_s \propto D_s \exp(-\Delta G_{\max}/k_B T) \quad (1)$$

where ΔG_{\max} denotes the main barrier in the respective PMF, T the temperature, and k_B the Boltzmann constant. The diffusion constant D_s of solute s is assumed to be proportional to an attempt frequency to overcome the barrier and should not imply that a local diffusion model holds.

The first set of such simulations started with a CO₂ at the position taken from the 3B9Z structure¹⁵ (Figure 1C). Figure 2C shows the z -coordinate of that CO₂ molecule during 6 independent 50 ns simulations of the NeRh50 trimer, yielding 18 independent CO₂ trajectories. The CO₂ molecules are remarkably stable at the X-ray position, with only one out of 18 CO₂ molecules escaping from the starting position within 50 ns (black curve in Figure 2C). The single CO₂ molecule which escapes from the 3B9Z CO₂ position diffuses further into the channel past the two conserved pore histidines, but does not cross the main barrier at Phe194 within the simulation time. The metastable CO₂ position is displaced by ~ 3 Å with respect to the nearby local minimum in the PMF (Figure 2A), possibly because the shorter umbrella simulations are not able to fully sample CO₂ positions in the binding pocket with respect to positions in the main pore.

For the second set of CO₂ diffusion simulations, 28 CO₂ molecules per NeRh50 monomer were placed into the bulk water close to the channel axis, and subsequently restrained into cylinders centered along the respective channel axis. Six such simulation systems were set up and simulated for 40 ns. The CO₂ trajectories of one typical representative of these six simulations are plotted in Figure 2D, and the trajectories from all six simulations are available as Figure S2 in the Supporting Information. As visible from the trajectories, multiple CO₂ molecules enter the pore, mainly via the low-barrier path from the cytoplasmic side (negative z). Subsequently, the molecules remain at the minima in the PMF for nanoseconds to tens of nanoseconds. Only two full permeation events are observed during the 240 ns of simulation (simulation 3 in Figure S2 in the Supporting Information) because the main barrier at the Phe194 is rarely crossed. Taken together with the simulations of CO₂ starting at the CO₂ position in the 3B9Z structure, these findings indicate that, although NeRh50 can be permeated by CO₂, NeRh50 is not a particularly efficient CO₂ channel, and the CO₂ located inside the channel according to the 3B9Z structure is surprisingly stable. Hence, CO₂ molecules at that position are temporarily immobilized and do not efficiently contribute to rapid CO₂ permeation.

For comparison, diffusion simulations of CO₂ across a lipid membrane composed of both POPE and POPC were carried out. To this end, 40 randomly chosen water molecules of a pre-equilibrated membrane patch were replaced by CO₂. The system was simulated 6 times for 50 ns with different starting velocities, yielding 300 ns of independent simulation. The CO₂ trajectories of one of the six simulations are plotted in Figure 2E. During 50 ns, 8 full permeation events across the bilayer were observed. Three of them are highlighted by thick curves in Figure 2E. In the entire set of 300 ns of simulation (Figure S3 in the Supporting Information), 45 permeation events were observed.

The number of semipermeation events across one membrane leaflet can be translated into an accurate membrane permeability (compare Methods), yielding a large permeability of $P_{\text{CO}_2}(\text{PE/PC}) = 3.0$ cm/s. Likewise, the single-channel permeability p_{CO_2} of NeRh50 can be estimated from partial CO₂ permeation events across the NeRh50 pore. Because of the substantial barrier, we observed many fewer permeation events as compared to the membrane simulations, allowing us only to compute the p_{CO_2} order of magnitude to $p_{\text{CO}_2} \approx 1 \times 10^{-14}$ cm³/s. Even when assuming the largest possible density of NeRh50 in the membrane (corresponding to a NeRh50 2-dimensional crystal), this value translates into a membrane permeability of only $P_{\text{CO}_2}(\text{NeRh50-dense}) \approx 0.1$ cm/s, 1–2 orders of magnitude smaller than $P_{\text{CO}_2}(\text{PE/PC})$. Hence, the diffusion simulations corroborate the conclusions from the PMFs, that NeRh50 is unlikely to contribute to CO₂ flux across membranes composed of POPE and POPC. Using eq 1, p_{CO_2} can be estimated from $P_{\text{CO}_2}(\text{PE/PC})$ and the difference between the NeRh50 and PE/PC barriers of 14.5 and 5.5 kJ/mol, respectively, yielding a $p_{\text{CO}_2} = 1 \times 10^{-14}$ cm³/s (67% confidence intervals of 0.5 and 2.3×10^{-14} cm/s), in agreement with the value derived directly from the diffusion simulations. This finding demonstrates that (i) the PMFs provide reliable permeability estimates assuming a simple rate ansatz (eq 1), directly connecting the dynamics of permeation to the underlying energetics, and (ii) the main barriers of the PMFs have not been underestimated by integrating out orthogonal degrees of freedom, such as motions of the pore-

Table 1. Summary of Free Energy Barriers and Permeabilities^a

	CO ₂	NH ₃
<i>Nitrosomonas europaea</i> Rh50		
barrier ΔG_{\max} [kJ/mol]	14.5 ± 2 ^b	17.5 ± 2 ^b
single-channel permeability [cm ³ /s]	~10 ⁻¹⁴ ^c /1 × 10 ⁻¹⁴ ^d	~5 × 10 ⁻¹⁵ ^c /3 × 10 ⁻¹⁵ ^d
<i>P</i> (RhAG density in human RBC ghosts) ^e [cm/s]	1 × 10 ⁻³ ^d	3 × 10 ⁻⁴ ^d
Lipid Membranes		
POPE/POPC barrier ΔG_{\max} [kJ/mol]	<6 ± 1 ^b	19.5 ± 1 ^b (PE)/13.5 ± 1 ^b (PC)
POPE/POPC permeability [cm/s]	3.0 ^c (PE:PC 1:1)	0.017 ^c (PE)/0.13 ^c (PC)
POPE/POPG 3:1 barrier ΔG_{\max} [kJ/mol]	9 ± 2 ^b	19 ± 2 ^b
POPE/POPC + 20–60 mol % cholesterol, ΔG_{\max} [kJ/mol]	5–19 ± 2 ^b	21–33 ± 2 ^b

^a The errors indicate 67% confidence intervals. ^b From umbrella sampling simulations. ^c From diffusion simulations. ^d Expected from eq 1 using lipid bilayer permeabilities and the difference between NeRh50 and lipid membrane barriers. ^e Assuming the NeRh50 density equal to the RhAG density in human red blood cells (RBCs), i.e. ~1000/μm².⁶

occluding Phe194 phenyl ring. The barrier heights and permeabilities determined from the simulations are summarized in Table 1.

Potentials of Mean Force for NH₃, NH₄⁺, Methylamine, and Water. Figure 4A displays the PMF for NH₃ translocation across NeRh50 as a black curve. The main barrier of 17.5 kJ/mol is *not* located near the pore-occluding Phe194 ($z \approx 0.8$ nm), but at a position between the two conserved pore histidines ($z \approx 0$ nm). At this site the channel is both hydrophobic and narrow, presumably rendering the position for NH₃ relatively unfavorable. Favorable positions for NH₃ are located next to His300 where NH₃ is stabilized through a hydrogen bond to the N_ε atom of the histidine ($z \approx -0.45$ nm), as well as at the positions below and above the pore-occluding Phe194 ($z \approx 0.45$ nm and $z \approx 1.2$ nm). The blue curve in Figure 4A presents the PMF for NH₄⁺ translocation along the pore. It is notable that NH₄⁺ can freely diffuse up to the hydrophilic extracellular vestibule at $z = 1.2$ nm surrounded by the carbonyl backbone atoms of Ser139 and Ala140, as well as by the hydroxyl group of Tyr118. The PMF of NH₄⁺ increases as NH₄⁺ approaches the Phe194 gate, supporting the proposition that it is the neutral form, NH₃, that is permeated by Rh50, in agreement with the pH-dependent methylamine uptake by NeRh50 observed in experiments.^{45,46} The green curve in Figure 4A presents the PMF for methylamine permeation across NeRh50, in excellent agreement with the NH₃ PMF and, hence, demonstrating that methylamine can be used as a model for NH₃ during permeation experiments.

To assess whether NeRh50 is capable of conducting water in addition to NH₃, we have computed the PMF for water translocation across the channel (Figure 4A, red curve). Remarkably, NeRh50 constitutes a 26 kJ/mol barrier against water permeation and therefore discriminates approximately 40-fold between water and ammonia. For comparison, the water channel aquaporin-1 constitutes only a barrier of 13 kJ/mol against water permeation²⁹ and therefore displays a 150-fold higher single-channel water permeability than NeRh50. In the simulations, the NeRh50 pore was only partially hydrated from the cytoplasmic side up to the position below His300 ($z \sim -0.5$ nm, compare Figure 1C) and from the periplasmic side up to the Phe194 gate. In accordance to the PMF, the channel was never fully hydrated during a 20 ns equilibrium simulation of NeRh50, as well as during the six 40 ns simulations in which CO₂ was allowed to diffuse across the channel (see above).

Figure 4B presents the PMFs for NH₃ permeation across the PE membrane (black curve), PC membrane (red curve), PE/PC membrane (green curve), and PE/PG membrane (magenta curve). In addition, the respective PMF for NH₄⁺ translocation across the PE membrane is shown as a blue curve. The heights of the main barriers for NH₃ translocation across the lipid membranes are of the same order of magnitude as for NH₃ translocation across the NeRh50 channel. Hence, in such membranes NeRh50 is not expected to enhance the NH₃ flux across the membrane. To assess whether cholesterol-containing membranes display different permeation characteristics, we have computed PMFs for NH₃ permeation across membranes with an increasing cholesterol content between 20 and 60 mol %. As shown in Figure 4E, cholesterol substantially increases the barrier. For a cholesterol content between 40 and 50 mol % for instance, the PMFs show a barrier of ~29 kJ/mol, which is ~12.5 kJ/mol higher than the barrier for NH₃ permeation across NeRh50. Assuming a NeRh50 expression density similar to the RhAG density in RBCs,⁶ that difference is sufficient to render NeRh50 a physiological NH₃ channel. Taken together, only in dense membranes such as membranes with substantial cholesterol content NeRh50 is expected to enhance the NH₃ flux.

Spontaneous NH₃ Permeation across NeRh50 and Lipid Membranes. As an independent assessment of NH₃ permeation across the pore and to yield insight into the diffusive contribution to NH₃ permeation, we have carried out MD simulations in which NH₃ could freely diffuse across the NeRh50 pore. Similarly, POPC and POPE membrane systems were simulated in which NH₃ was allowed to diffuse freely. The setup of the NeRh50 diffusion simulations was identical to the CO₂ simulations discussed above (Figures 2D/E), except that CO₂ molecules were replaced by NH₃ molecules. Accordingly, six independent 40 ns simulations of the NeRh50 trimer were carried out, each simulation containing 28 NH₃ molecules per NeRh50 monomer. The NH₃ trajectories of one of the six NeRh50 simulations are shown in Figure 4C; the NH₃ trajectories from all six simulations are available as Figure S4 in the Supporting Information. During the complete set of 240 ns of simulation, one full permeation event was observed (black curve in Figure 4C), together with multiple partial permeation events (e.g., green and red curves in Figure 4C, see also Figure S4 in the Supporting Information). That finding demonstrates that the Rh50 crystal structure represents a functional form of NeRh50, and that no structural transitions or even additional proteins are required to allow NH₃ permeation. The limited number of permeation events suggest, however, that NeRh50 is only a moderately effective channel, consistent with the substantial barriers in the PMF (Figure 4A).

(45) Cherif-Zahar, B.; Durand, A.; Schmidt, I.; Hamdaoui, N.; Matic, I.; Merrick, M.; Matassi, G. *J. Bacteriol.* **2007**, *189*, 9090–9100.

(46) Weidinger, K.; Neuhäuser, B.; Gilch, S.; Ludewig, U.; Meyer, O.; Schmidt, I. *FEMS Microbiol. Lett.* **2007**, *273*, 260–267.

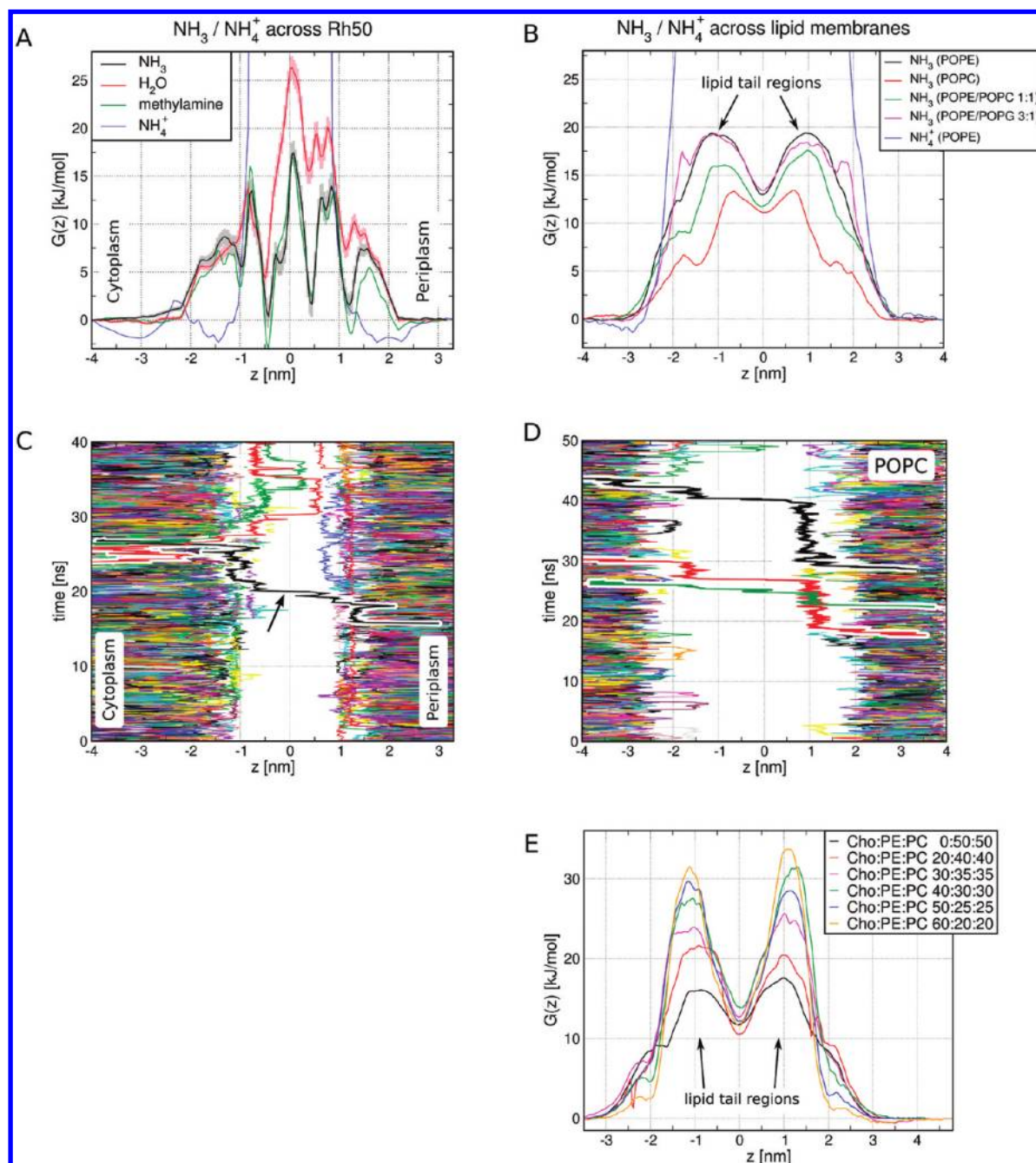


Figure 4. $\text{NH}_3/\text{NH}_4^+$ permeation across the NeRh50 channel and lipid membranes. (A) Potentials of mean force (PMF) for NH_3 , water, and methylamine permeation across NeRh50 (black, red, and green curves, respectively). Statistical uncertainties (67% confidence interval) are indicated by shaded areas. The PMF for NH_4^+ translocation along the NeRh50 pore is plotted as a blue curve. (B) PMFs for NH_3 permeation through lipid membranes composed of pure POPE (black), pure POPC (red), an equal mixture of POPE and POPC (green), and of a 3:1 mixture of POPE and POPG (magenta). The blue curve shows the PMF for NH_4^+ translocation perpendicular to the membrane. (C) Trajectories of free (unrestrained) NH_3 molecules partially permeating across NeRh50 as derived from a 40 ns simulation. (D) Trajectories of free NH_3 molecules permeating across the lipid membrane composed pure POPC (red PMF in B). Three full permeation events are highlighted as thick black, red and green lines. For visualization, all trajectory curves were slightly smoothed by running averages. NH_3 trajectories derived from additional independent simulations of both NeRh50 and POPC membranes are available as Supporting Information. (E) Influence of cholesterol on the NH_3 permeability of lipid membranes. Potentials of mean force (PMFs) of NH_3 permeation across membranes containing an equal mixture of POPE and POPC plus and increasing cholesterol content of 0, 20, 30, 40, 50, and 60 mol %.

To derive the NH_3 permeability of PE and PC, multiple MD simulations of both systems were carried out with different initial velocities, yielding 500 ns (385 ns) of simulation of the POPC (POPE) system. The NH_3 trajectories of 50 ns of the POPC system are plotted in Figure 4D. Three complete permeation events are highlighted as thick black, red, and green curves. The NH_3 trajectories from the complete 500 ns of POPC

simulation are shown in Figure S5 in the Supporting Information. In total, 17 full permeation events across the POPC membrane were observed (Figure S5 in the Supporting Information), and two full permeation events across the POPE membrane (not shown).

Following the analysis carried out for CO_2 (see above), the number of semipermeation events across one membrane leaflet

translates into membrane permeabilities of 0.13 and 0.017 cm/s for the PC and PE membranes, respectively, in reasonable agreement with experimental estimates for similar membranes. An NH_3 permeability of 0.13 cm/s was reported for egg PC/decane membranes,⁴⁷ and 0.048 cm/s for diphytanoyl PC.⁴⁸ The single-channel NeRh50 permeability for NH_3 is slightly lower than that for CO_2 , that is $p_{\text{NH}_3} \approx 5 \times 10^{-15}$ cm³/s. To assess the consistency between PMFs and diffusion simulation, p_{NH_3} can be computed via eq 1 using the PC membrane permeabilities, together with the barriers in the respective PMFs (compare Methods). From that analysis, $p_{\text{NH}_3} = 3 \times 10^{-15}$ cm³/s is expected, in reasonable agreement with the estimate from the diffusion simulation.

Permeation through the Central Pore Is Unfavorable. The role of human aquaporin-1 (AQP1) as a physiological CO_2 channel has been controversially discussed for more than a decade^{25,28,49–52} and seems still not resolved, mainly because the measurement of the intrinsic membrane permeabilities for CO_2 is challenging in the presence of unstirred layers.²⁶ Simulations showed that the free-energy barrier for CO_2 translocation across the hydrophobic central pore of AQP1 (along the tetrameric axis) is substantially lower than the respective barrier for the water pores,²⁹ which led to speculations that the AQP1 central pore is a relevant CO_2 channel.^{10,52} Because the monomeric pores of NeRh50 constitute a substantial barrier against CO_2 permeation (Figure 2), we tested whether the central pore of NeRh50 might contribute to CO_2 flux. Figure 5A shows a molecular representation of the NeRh50 central pore, and Figure 5B the PMF for CO_2 permeation across the central pore (black curve). The PMF displays several large barriers of up to 45 kJ/mol against CO_2 permeation, mainly caused by tight packing of the side chains of Ala11 ($z = 2.5$ nm), Val14 ($z = 2.0$ nm), and Leu182 ($z = -0.7$ nm). In addition, Figure 5B presents the PMF for NH_3 permeation across the central pore (red curve), displaying equally high barriers as the CO_2 PMF. From the PMFs we can exclude any significant role of the central pore as a CO_2 or NH_3 channel.

The central pore of the recently resolved structure of RhCG¹⁶ is more open in the region corresponding to the high barriers in Figure 5B, implying that these barriers may be lower in RhCG. However, the lower part of the central pore ($z < 0$ nm) of RhCG is similar to NeRh50. Here, the PMF constitutes barriers on the order of 20 and 30 kJ/mol against CO_2 and NH_3 permeation, respectively, rendering any permeation across the RhCG central pore unlikely.

Discussion

We have carried out extensive MD simulations to derive the energetics and dynamics of full permeation events across the NeRh50 channel, a close homologue of human Rh50 channels. Such simulations provide a well-controlled system and are thus suited to complement experimental efforts. Because simulations

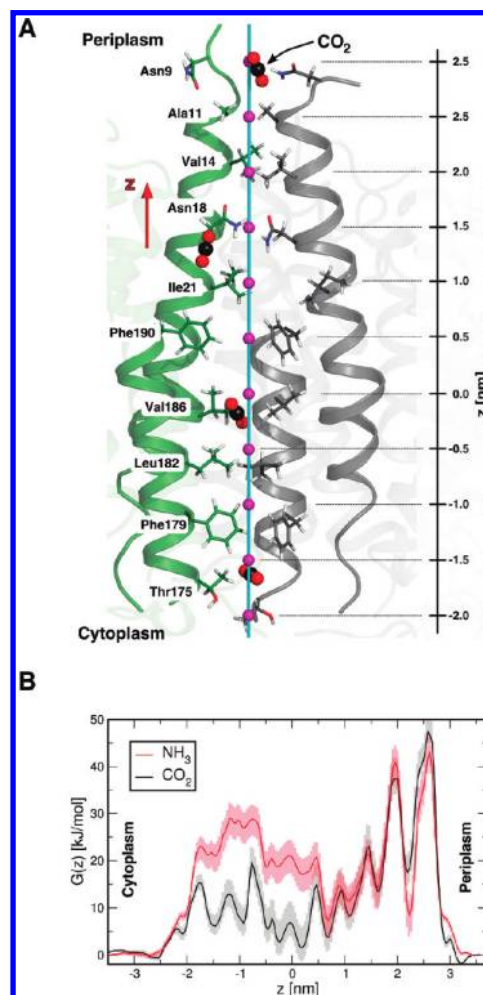


Figure 5. Energetics of CO_2 and NH_3 permeation through the central pore. (A) A snapshot of umbrella sampling simulation, showing the central pore of NeRh50. Helices 1 and 6 of monomer A (green) and monomer B (gray) are shown in cartoon representation, and some amino acid side chains aligning the central pore are depicted as sticks. CO_2 molecules are presented as spheres. For clarity, monomer C is not shown. (B) PMFs for CO_2 (black) and NH_3 (red) permeation through the central pore. 67% confidence intervals are indicated by shaded areas. Large barriers of more than 40 kJ/mol render any physiological role of the central pore as CO_2 or NH_3 channel unlikely.

may be biased by limited sampling or the applied force field, comparisons to quantitative experiments are mandatory wherever possible. However, quantitative comparisons to functional studies of Rh50 require care. Most functional experiments of Amt/Rh proteins have been carried out using cellular systems. Unfortunately they are plagued by a number of problems which include expression in heterologous systems, possible interference by other proteins, unstirred layer effects, or rather indirect assays for assessing substrate transport. Reconstituted systems using purified proteins (proteoliposomes) have yielded contradictory data on whether *Escherichia coli* AmtB functions as an NH_3 channel,^{11,20} but very recently have confirmed that human RhCG is active as an NH_3 channel.⁵³

We have applied MD simulations to compute PMFs for NH_3 , CO_2 , NH_4^+ , methylamine, and water permeation across the

- (47) Walter, A.; Gutknecht, J. *J. Membr. Biol.* **1986**, *90*, 207–217.
 (48) Antonenko, Y. N.; Pohl, P.; Denisov, G. A. *Biophys. J.* **1997**, *72*, 2187–2195.
 (49) Yang, B.; Fukuda, N.; van Hoek, A.; Matthey, M. A.; Ma, T.; Verkman, A. S. *J. Biol. Chem.* **2000**, *275*, 2686–2692.
 (50) Hub, J. S.; Grubmüller, H.; de Groot, B. L. *Handb. Exp. Pharmacol.* **2009**, *190*, 57–76.
 (51) Endeward, V.; Musa-Aziz, R.; Cooper, G. J.; Chen, L.-M.; Pelletier, M. F.; Virkki, L. V.; Supuran, C. T.; King, L. S.; Boron, W. F.; Gros, G. *FASEB J.* **2006**, *20*, 1974–1981.
 (52) Musa-Aziz, R.; Chen, L.-M.; Pelletier, M. F.; Boron, W. F. *Proc. Natl. Acad. Sci. U.S.A.* **2009**, *106*, 5406–5411.

- (53) Mouro-Chanteloup, I.; Cochet, S.; Chami, M.; Genetet, S.; Zidi-Yahiaoui, N.; Engel, A.; Colin, Y.; Bertrand, O.; Ripoche, P. *PLoS One* **2010**, *5*, e8921.

NeRh50 channel and across lipid membranes. In order to relate the PMFs to permeabilities and, hence, to facilitate the comparison to experiments, the PMFs have been complemented by diffusion simulations in which NH_3 and CO_2 molecules were allowed to spontaneously permeate across NeRh50 or across lipid bilayer membranes. The NeRh50 single-channel permeabilities derived from the diffusion simulations agree favorably with the values computed via eq 1 using the membrane permeabilities and the difference between the NeRh50 and membrane barriers (Table 1). Likewise, the relative membrane permeabilities are in accordance to the barriers in the PMFs. For instance, the NH_3 permeabilities of the PE and PC membranes can be estimated from the CO_2 permeability of the PE/PC membrane (3 cm/s), using eq 1 and the respective barriers. The calculation yields NH_3 permeabilities of 0.18 and 0.016 cm/s for the PC and PE membranes, respectively, in reasonable agreement with the values of 0.13 and 0.017 cm/s derived from the diffusion simulations. Hence, the PMFs and the permeabilities are internally consistent, strongly suggesting that the permeabilities of the other membranes can be estimated from the PMFs using eq 1. Note, however, that PMFs in Figures 2F and 4E correspond to the respective local cholesterol content. A high cholesterol content may trigger raft formation and, consequently, membrane domains with a lower cholesterol content (and lower barrier) could induce a higher overall membrane permeability.

To assess if NeRh50 substantially contributes to the flux of CO_2 or NH_3 across a certain membrane, the intrinsic channel and membrane permeabilities and the expression density of the channel must be considered. The NeRh50 barriers shown in Figures 2A and 4A correspond to a channel density of one channel per membrane cross section area A_{mono} occupied by one NeRh50 monomer or, equivalently, to a NeRh50 2D crystal. At finite expression level an additional entropic barrier must be added to the PMFs that accounts for the lower probability of the solute to “find” the channel. Given one NeRh50 monomer per membrane area A_1 , that entropic correction reads $\Delta G_A = -k_B T \ln(A_{\text{mono}}/A_1)$. For RhAG in human RBCs, for instance, Ripoché et al. reported the RhAG copy number of 80,000 and RBC ghost surface area of $\sim 80 \mu\text{m}^2$, corresponding to a density of $1000/\mu\text{m}^2$ and translating into $\Delta G_A = 10.9 \text{ kJ/mol}$. A substantial contribution of the channel to the solute flux is therefore only expected if the membrane barrier is at least 10 kJ/mol higher than the respective NeRh50 or RhAG barrier.

Because the putative role of NeRh50 as CO_2 channel critically depends on the permeability of the surrounding membrane, we have computed the PMFs for CO_2 permeation across a large set of lipid membranes, composed of either pure lipids or lipids plus an increasing cholesterol content. We found that membranes containing exclusively PE and PC head groups are highly permeable to CO_2 , with a barrier $< 6 \text{ kJ/mol}$ and a respective permeability of $> 3 \text{ cm/s}$ (Figure 2B/E). The anionic head groups of the PG lipids, as present in bacterial membranes, increase the CO_2 barrier to 9 kJ/mol and, hence, reduce the permeability to $\sim 0.6 \text{ cm/s}$. An increasing cholesterol content substantially reduces the membrane permeability. However, all CO_2 membrane barriers computed for the present study are substantially lower than the respective NeRh50 barrier at a channel density similar to RhAG in RBCs, even for membranes with a high cholesterol content. Hence, any role of NeRh50 as a CO_2 channel seems unlikely in such membranes. The CO_2 permeability of lipid membranes is still controversial, mainly because the measurement of the bare membrane permeability is chal-

lenging in the presence of unstirred layers. Recently, Missner et al. estimated a permeability of 3 cm/s for cholesterol-containing membranes²⁵ and Endeward et al. reported a basal permeability of 0.015 cm/s for the RBC membrane,¹⁰ whereas earlier studies by Gutknecht and co-workers reported a bilayer CO_2 permeability of 0.35 cm/s.⁵⁴ We cannot resolve here whether these discrepancies are related to unstirred-layer effects, or different lipid composition and cholesterol content. However, even the low value reported by Endeward et al. corresponds to a barrier of $\sim 19 \text{ kJ/mol}$, which would be still too low to render NeRh50 a relevant CO_2 channel.

Experiments that assess the CO_2 flux across membranes are typically carried out in the presence of carbonic anhydrase (CA) to accelerate the $\text{CO}_2/\text{HCO}_3^-$ equilibration. At present there are no indications that Rh50—similar to CA—modulates the $\text{CO}_2/\text{HCO}_3^-$ equilibration. However, we cannot exclude such a mechanism in Rh50, which, consequently, could indirectly affect the apparent CO_2 permeation rate.

The Rh50 channel has also been suggested to play a role in CO_2 transport across bacterial membranes.⁷ The lipid compositions of many bacterial membranes are unknown, and, hence, on the basis of the simulations presented here we can only draw limited conclusions on the role of NeRh50 in bacterial CO_2 transport. In particular, little is known about the lipid composition of *N. europaea*. However, *N. europaea* encodes a gene implicated in hopanoid synthase. Hopanoids play a role as membrane rigidifiers similar to sterols in animals and are thus expected to reduce the membrane permeability. In contrast to aerobic ammonia oxidizers such as *N. europaea*, anaerobic ammonia oxidizers have been studied in more detail. These microbes synthesize unusual lipids called ladderanes, which have likewise been shown to reduce the membrane permeability.⁵⁵ Because it is unclear to which extent hopanoids and possibly ladderane lipids reduce the CO_2 permeability of *N. europaea* membranes, more experimental research will be required to fully resolve the role of NeRh50 as bacterial CO_2 channel. We can only exclude relevant Rh50-mediated CO_2 flux across the PE/PG membrane, which resembles the membranes found in *E. coli*. In addition, the PMFs suggest that Rh50 is only expected to contribute to CO_2 flux in exceptionally dense membranes that constitute a barrier well above 20 kJ/mol against CO_2 , corresponding to a permeability well below 0.01 cm/s.

Compared to the barriers in the CO_2 membrane PMFs, the more hydrophilic nature of NH_3 increases the barriers by roughly 15 kJ/mol in the hydrophobic core of the lipid membranes (Figures 2B/F, 4B/E), as expected from the difference in the hexadecane/water partition coefficients of 2.2×10^{-3} vs 1.5 for NH_3 and CO_2 , respectively. In contrast, the main NH_3 barrier for permeation across NeRh50 is only 3 kJ/mol higher than the respective CO_2 barrier. Consequently, NeRh50 substantially enhances the NH_3 flux across moderately dense membranes, in which NeRh50 hardly influences the CO_2 flux. The PMFs for methylamine and NH_3 permeation across Rh50 are very similar, suggesting similar methylamine and NH_3 permeabilities. Because of the higher $\text{p}K_a$ value of methylammonium (10.64 versus 9.25 at 25 °C), the flux of the neutral form in response to an equal gradient in the ionic form is expected to be approximately 25-fold lower for methylamine compared to NH_3 .

(54) Gutknecht, J.; Bisson, M. A.; Tosteson, F. C. *J. Gen. Physiol.* **1977**, *69*, 779–794.

(55) Rattray, J. E.; van de Vossenberg, J.; Hopmans, E. C.; Kartal, B.; van Niftrik, L.; Rijpstra, W. I. C.; Strous, M.; Jetten, M. S. M.; Schouten, S.; Damsté, J. S. *Arch. Microbiol.* **2008**, *190*, 51–66.

Very recently, the structure of the human RhCG protein was resolved.¹⁶ An overlay of the NeRh50 and RhCG structures shows a high degree of similarity, and in particular the pore residues are highly conserved. The results that were derived here from the *N. europaea* Rh50 structure are therefore expected to hold qualitatively as well for human Rh50 channels such as RhCG. RhCG was recently reconstituted into liposomes, yielding a so-called “apparent” NH₃ single-channel permeability of about 1×10^{-15} cm³/s at a temperature of 8 °C.⁵³ Note that the apparent NH₃ permeability is defined from the NH₃ flux in response to an NH₄⁺ gradient. Measurements in RBCs and HEK cells suggested apparent NH₃ permeabilities of 2.18×10^{-15} cm³/s and 1.6×10^{-15} cm³/s, respectively (at 15 °C).^{6,17} Assuming (i) that NH₃ is the only permeating species and (ii) equilibrium between NH₃ and NH₄⁺ in the extracellular medium, these apparent NH₃ permeabilities can be translated into NH₃ permeabilities, that is into the NH₃ flux in response to an NH₃ gradient. The experiments were carried out at pH 6.8 and 8 °C⁵³ ($pK_a = 9.92^{56}$), and at pH 7.0 and 15 °C^{6,17} ($pK_a = 9.68$), respectively, implying very high NH₃ permeabilities of $\sim 1 \times 10^{-12}$ cm³/s. This value is between 2 and 3 orders of magnitude larger than the permeability derived from our simulations and can hardly be explained by some experimental uncertainties like for example in the estimated channel density.

For comparison, the NH₃ permeability of aquaporin-8 equals $5\text{--}10 \times 10^{-14}$ cm³/s.⁵⁷ The aquaporin-8 pore is, however, not purely hydrophobic, also allowing rapid water flux. Thus, aquaporin-8 is expected to exhibit a higher NH₃ permeability as compared to the purely hydrophobic Rh50 pore, in line with the low NH₃ barrier of 12.5 kJ/mol that we found for the aquaglyceroporin GlpF in a previous study.³² Nevertheless, to verify that the umbrella sampling simulations have not overestimated the main barrier for NH₃ permeation across Rh50 because of poor convergence, we have computed the respective PMF for each monomer separately (Figure S5A in the Supporting Information). The main barriers near the twin histidines ($z = 0$ nm in Figure 4A) differ by less than 1 kJ/mol between the three Rh50 monomers, suggesting that the PMFs are converged. In addition, we have computed Rh50 PMFs using two alternative protonation states of the twin histidines His146 and His300 (Figure S5B/C in the Supporting Information). However, the alternative histidine protonation did not reduce the barrier in the NH₃ PMFs, indicating that uncertainties in the histidine protonation do not account for the discrepancy from ref 53.

We stress that the comparison between our simulations and flux measurements may be impeded by the diffusion of NH₄⁺ across possible unstirred layers on both sides of the membrane as well as by multiple (de)protonation steps in the experiment. In addition, permeation measurements must (by definition) be carried out under nonequilibrium, whereas we here derived permeabilities from equilibrium simulations. Could such additional permeation steps, nonequilibrium effects, or even multiparticle effects account for the different NH₃ permeabilities? The accumulation of multiple NH₃ in the pore causing a knock-on mechanism, that could theoretically enhance the rate as compared to the single-molecule scenario, was not observed in the diffusion simulations, which were carried out at high NH₃ concentration. Likewise, additional rate-limiting permeation

steps, such as slow deprotonation of NH₄⁺ or significant unstirred layer effects, would be expected to imply an even higher experimental NH₃ permeability of Rh50. Therefore it seems unlikely that physiological ammonia/ammonium and pH gradients under steady state (nonequilibrium) flux conditions can enhance the effective ammonia permeability by several orders of magnitude, thereby explaining the high experimentally observed effective ammonia permeation rate.⁵³ Thus, although our simulations qualitatively agree with the experiments by demonstrating the role of Rh50 as ammonia channel, we cannot resolve the apparent quantitative discrepancy at present but suggest further theoretical studies as well as additional quantitative flux experiments on Rh50 proteins, possibly using reconstitution into planar lipid membranes. To complement the equilibrium situation studied here, it will be interesting to address by future simulation studies the physiological/experimental situation under steady-state flux conditions following a NH₄⁺ gradient, and explicit (de)protonation effects to include the NH₄⁺ to NH₃ interconversion.

NeRh50 poses a substantial barrier of 26 kJ/mol against the permeation of water, suggesting a single-channel permeability of $\sim 1 \times 10^{-16}$ cm³/s. Thus, NeRh50 displays a ~ 40 -fold lower water as compared to NH₃ permeability, in accordance with measurements on proteoliposomes and human RBC that did not exhibit Rh-dependent water permeability.^{6,53} Interestingly, NeRh50 has different permeability characteristics from both aquaporins and aquaglyceroporins (AQPs). Whereas aquaporins facilitate rapid water flux but exclude NH₃, aquaglyceroporins such as AQP8 or GlpF allow the permeation of both water and NH₃.^{32,57,58} Rh50 channels complement AQPs by exhibiting moderate NH₃ but low water permeability.

Conclusions

The extensive molecular dynamics (MD) trajectories presented here show that the 50 kDa Rhesus protein channel Rh50 is functional in its crystallographic conformation, allowing ammonia (NH₃) as well as carbon dioxide (CO₂) molecules to pass by thermal diffusion, without the requirement for a conformational change or the action of any protein partner. Significant solute flux across Rh50 is only expected if the channel constitutes a lower barrier against solute permeation than the surrounding lipid membrane. To assess the physiological relevance for CO₂ and NH₃ permeation across Rh50, we have therefore computed potentials of mean force (PMFs) for CO₂ and NH₃ permeation across Rh50 and a large set of lipid membranes. The PMF calculations were complemented by simulations that allowed the spontaneous diffusion of CO₂ and NH₃ across Rh50 and lipid membranes, yielding a direct estimate for single-channel and membrane permeabilities. These simulations are quantitatively consistent with the PMFs, suggesting that the heights of the main PMF barriers are the key determinants for channel and membrane permeabilities, whereas other properties (such as the shape of the PMF) play a minor role. The consistency between diffusion simulations and PMFs as well as the agreement with experimental membrane permeabilities validates the potential of current MD simulation techniques, whereas remaining discrepancies from experiments may indicate where methodological improvements, both theoretical and experimental, may still be needed. The PMFs demonstrate that an increasing cholesterol content reduces the

(56) Khoo, K. H.; Culbertson, C. H.; Bates, R. G. *J. Solution Chem.* **1977**, *6*, 281–290.

(57) Saparov, S. M.; Liu, K.; Agre, P.; Pohl, P. *J. Biol. Chem.* **2007**, *282*, 5296–5301.

(58) Beitz, E.; Wu, B.; Holm, L. M.; Schultz, J. E.; Zeuthen, T. *Proc. Natl. Acad. Sci. U.S.A.* **2006**, *103*, 269–274.

intrinsic membrane permeability for both CO₂ and NH₃. In contrast, the addition of the anionic lipids to a membrane of zwitterionic lipids reduces the CO₂, but hardly affects the NH₃ permeability. The PMFs for solute permeation across the Rh50 channel suggest that Rh50 substantially contributes to NH₃ flux in dense membranes such as membranes with a high cholesterol content. Despite the reduced CO₂ permeability of cholesterol-containing membranes, the CO₂ permeabilities of all membranes studied here are still too high to allow for significant Rh50-mediated CO₂ flux. Rh50 is only expected to contribute to CO₂ flux across membranes with an exceptionally low intrinsic CO₂ permeability with a barrier well above 20 kJ/mol. Rh50 channels exhibit a very low water permeability and therefore show different characteristics than aquaglyceroporin channels, which facilitate the flux of both water and ammonia.

Methods

Simulation Setup. The NeRh50 simulations were set up as follows. The initial NeRh50 structure was taken from the protein data bank (PDB code 3B9W¹⁴). The protonation states of the histidine residues were estimated using the WHAT IF modeling software.⁵⁹ As a result, His146 acted as hydrogen bond donor toward His300. Crystal water was kept in the structure, and the protein was placed into a simulation box of a hexagonal prism. The protein was solvated in a lipid membrane of pure POPE using the make-hole version of Gromacs.⁶⁰ Water molecules were added to the system, and the system was neutralized by adding 48 sodium and 30 chloride ions, corresponding to an approximate electrolyte concentration of 150 mM. In total, the simulation system included the NeRh50 trimer, 298 POPE lipids, 13570 water molecules, and the electrolyte, summing up to a total of 86105 atoms. The system was energy minimized using a conjugate gradient algorithm. To allow the lipids to fully equilibrate around the protein surface, the system was subsequently simulated for 70 ns with position restraining potentials ($k = 1000$ kJ/mol/nm²) on the backbone atoms of NeRh50. A typical simulation box is shown in Figure 1A/B.

All simulations were carried out using the Gromacs simulation software.^{61,62} The OPLS all-atom force field^{63,64} and the TIP4P model⁶⁵ were employed for the protein and water, respectively, and lipid parameters were taken from refs 66 and 67. Ammonia and CO₂ parameters were taken from refs 64 and 29, respectively. In a previous study these parameters have been validated by reproducing the experimental hexadecane/water partition coefficients K_{hex} .³² Parameters for methylamine (MA) were taken from the OPLS forcefield and were accordingly validated by reproducing K_{hex} using the umbrella sampling procedure applied in ref 32. $K_{\text{hex}}(\text{MA}) = 4.9 \times 10^{-3}$ was found, in favorable agreement with the experimental value of 5.5×10^{-3} .⁴⁷ Electrostatic interactions were calculated at every step with the particle-mesh Ewald method.^{68,69} Short-range repulsive and attractive dispersion interactions were described together by a Lennard-Jones potential, which

was cut off at 1.0 nm. The Settle⁷⁰ algorithm was used to constrain bond lengths and angles of water molecules, and LINCS⁷¹ was used to constrain all other bond lengths, allowing a time step of 2 fs. The simulation temperature was kept constant at 300 K by coupling the system to a Nosé–Hoover thermostat^{72,73} ($\tau = 2$ ps). Likewise, the pressure was kept at 1 bar using the Parrinello–Rahman pressure coupling scheme⁷⁴ ($\tau = 5$ ps). During umbrella simulations only, the box length in the z direction (perpendicular to the membrane) was kept fixed to avoid possible artifacts in the umbrella histograms. The energy of the hydrogen bond between Phe194 and water was estimated using the relation proposed by Espinosa et al.⁷⁵

The lipid membrane simulations were carried out by starting from pre-equilibrated patches of POPE and POPC. The POPE and the POPC patch contained 128 lipid molecules each and 4777 or 5788 TIP4P water molecules, respectively. The mixed POPE/POPC patch and patches containing cholesterol were constructed by placing single lipid or cholesterol molecules randomly distributed on a square grid for each monolayer, yielding a lipid bilayer that contained at least 128 lipid or cholesterol molecules. An equilibrated structure for the POPE/POPG membrane was taken from Zhao et al.⁶⁷ and contained 96 POPE, 16 l-POPG, 16 d-POPG, and 32 sodium ions. The membranes were solvated with at least 3293 TIP4P water molecules. The POPE/POPC system was thermalized during a 25 ns equilibrium simulation, and the membranes containing cholesterol during simulations of at least 180 ns. The equilibration was checked from the potential energy and the box dimensions. Cholesterol parameters were taken from Höltje et al.⁷⁶ All simulation parameters were identical to the NeRh50 simulations. A typical membrane simulation box is shown Figure 1D.

Umbrella Sampling Simulations. The starting frames for the umbrella simulations were taken each from the first 1.5 ns of an equilibrium simulations of NeRh50, skipping the first 0.5 ns for equilibration. We chose to select the starting frames from a short simulation because such conformations are close to the high-resolution (1.3 Å) X-ray structure and thus supported by experimental data. The NeRh50 channels were divided into 0.1 Å wide equidistant sections parallel to the membrane with the center of each section representing an umbrella center. Because the pore of NeRh50 is not straight, the x – y position of the pore as a function of z was computed by HOLE⁷⁷ (cyan tube in Figure 1C). For the HOLE run only, the phenyl ring of the pore-occluding Phe194 was removed from the structure. The solute was placed into the pore at the umbrella center. For the umbrella simulations along the central pore of NeRh50, the solutes were placed at the center of mass (COM) of the NeRh50 trimer in the xy plane. Water molecules that overlapped with the solute were removed. To enhance sampling, four to five solute molecules were placed in each pore at different z positions, keeping a distance of at least 15 Å between the solutes.

Each umbrella sampling simulation was carried out by applying a harmonic restraint force along the pore coordinate with a force constant of 800 kJ/mol/nm². In ammonia the nitrogen atom was restrained, in water the oxygen, in CO₂ the carbon atom, and in methylamine a dummy atom centered between the carbon and nitrogen atom. Additionally, the solutes were restrained to a cylinder of radius $r_c = 5$ Å whose axis was centered along the pore by applying a flat-bottom quadratic potential in the xy plane. That potential was implemented by an additional force $F(r) = -k_c(r - r_c)H(r - r_c)$ pointing toward the cylinder axis. Here, r denotes the

(59) Vriend, G. *J. Mol. Graphics* **1990**, *8*, 52–56.

(60) Faraldo-Gómez, J. D.; Smith, G. R.; Sansom, M. S. P. *Eur. Biophys. J.* **2002**, *31*, 217–227.

(61) Van der Spoel, D.; Lindahl, E.; Hess, B.; Groenhof, G.; Mark, A. E.; Berendsen, H. J. C. *J. Comput. Chem.* **2005**, *26*, 701–1719.

(62) Hess, B.; Kutzner, C.; van der Spoel, D.; Lindahl, E. *J. Chem. Theory Comput.* **2008**, *4*, 435–447.

(63) Jorgensen, W. L.; Maxwell, D. S.; Tirado-Rives, J. *J. Am. Chem. Soc.* **1996**, *118*, 11225–11236.

(64) Kaminski, G. A.; Friesner, R. A.; Tirado-Rives, J.; Jorgensen, W. L. *J. Phys. Chem. B* **2001**, *105*, 6474–6487.

(65) Jorgensen, W. L.; Chandrasekhar, J.; Madura, J. D.; Impey, R. W.; Klein, M. L. *J. Chem. Phys.* **1983**, *79*, 926–935.

(66) Berger, O.; Edholm, O.; Jähnig, F. *Biophys. J.* **1997**, *72*, 2002–2013.

(67) Zhao, W.; Róg, T.; Gurtovenko, A. A.; Vattulainen, I.; Karttunen, M. *Biophys. J.* **2007**, *92* (4), 1114–1124.

(68) Darden, T.; York, D.; Pedersen, L. *J. Chem. Phys.* **1993**, *98*, 10089–10092.

(69) Essmann, U.; Perera, L.; Berkowitz, M. L.; Darden, T.; Lee, H.; Pedersen, L. G. *J. Chem. Phys.* **1995**, *103*, 8577–8592.

(70) Miyamoto, S.; Kollman, P. A. *J. Comput. Chem.* **1992**, *13*, 952–962.

(71) Hess, B. *J. Chem. Theory Comput.* **2008**, *4*, 116–122.

(72) Nosé, S. *Mol. Phys.* **1984**, *52*, 255–268.

(73) Hoover, W. G. *Phys. Rev. A* **1985**, *31*, 1695–1697.

(74) Parrinello, M.; Rahman, A. *J. Appl. Phys.* **1981**, *52*, 7182–7190.

(75) Espinosa, E.; Molins, E.; Lecomte, C. *Chem. Phys. Lett.* **1998**, *285*, 170–173.

(76) Höltje, M.; Förster, T.; Brandt, B.; Engels, T.; von Rybinski, W.; Höltje, H. D. *Biochim. Biophys. Acta* **2001**, *1511*, 156–167.

distance from the cylinder axis, $k_c = 400$ kJ/mol/nm² the force constant, and H the Heaviside step function. After energy minimization, each umbrella simulation was carried out for 500 ps.

Umbrella simulations for the lipid bilayers were set up by subdividing the membrane into 0.25 Å equidistant umbrella windows. The solute molecules were inserted into random snapshots taken from a 20 ns equilibrium run of the bilayer patch. Up to 12 solute molecules were inserted into one simulation, keeping a minimum distance of 20 Å from each other parallel and perpendicular to the bilayer. After energy minimization the simulations were carried out for 500 ps (1 ns for cholesterol-containing membranes) using umbrella potential constants between 400 and 4000 kJ/mol/nm².

Construction of PMFs. After removing the first 100 ps for equilibration (500 ps for cholesterol-containing membranes), umbrella histograms were extracted from the z -coordinate of the restrained atom. Subsequently, the umbrella positions were corrected with respect to the average COM of the corresponding NeRh50 monomer during the umbrella simulation, or, in the case of a lipid membrane simulation, with respect to the COM of all lipids. This procedure transforms the reaction coordinate from the absolute z -coordinate to the z -coordinate relative to the COM of the respective monomer (or lipid membrane). It avoids a possible unphysical flattening of the PMF due to different z -coordinates of the monomer COMs (or of the membrane COM) in the initial frames for the umbrella simulations. The COM of the NeRh50 monomers and lipid membranes fluctuated by only ± 0.2 Å during the umbrella simulations, implying that restraining the solutes at absolute z , complemented by the subsequent COM correction, allows for accurate sampling of the PMF barriers. 2190 histograms were collected for each PMF for permeation through the NeRh50 monomeric pores, 1155 histograms for each central pore PMF, and 1280 histograms for each membrane PMF.

The PMFs were computed using a periodic implementation of the weighted histogram analysis method (WHAM). The WHAM procedure incorporated the integrated autocorrelation times (IACT) of the umbrella windows, according to the WHAM equations derived by Kumar et al.⁷⁸ The IACTs were derived by fitting a double exponential to the autocorrelation function of each window, allowing one to analytically compute the IACTs. Because the IACT is subject to large uncertainty in the case of limited sampling (such as inside the channel), we have subsequently smoothed the IACT along the reaction coordinate using a moving average filter with a width of 5 Å. We found that taking account of the IACTs during WHAM has only a minor effect on the shape and barrier height of the profile. However, it avoids artifacts of a periodic WHAM such as a possible unphysical slope in the PMF in the (well-sampled) bulk water regions.

Due to the cylindrical restraint the umbrella samplings yield a PMF which refers to channel density of one channel per cross section of the cylinder. We corrected the PMFs by a trapezoidal correction in the entrance and exit regions of the pore such that the final PMFs refer to a density of one channel per membrane area occupied by an NeRh50 monomer. This correction allows a direct comparison between the NeRh50 PMFs and the membrane PMFs. The correction reads $\Delta G_{\text{cyl}} = k_B T \ln(A_{\text{mono}}/A_C)^{79}$ where A_{mono} denotes the membrane cross section of the NeRh50 monomer, A_C the effective membrane cross section of the cylinder, T the temperature and k_B the Boltzmann constant. A_C was chosen such that the entropy of the solute in the flat-bottom quadratic potential equals the entropy of a solute in a cylindrical well-potential of area A_C . We found that this condition approximately holds if A_C is computed via $A_C = \pi(r_c + 2\sigma_c)^2$ where $\sigma_c = (k_B T/k_c)^{1/2}$ is the width of the Gaussian-

shaped solute distribution at the edge of the flat-bottom quadratic potential. A_{mono} was estimated to equal 12.7 nm², and A_C was computed to 1.36 nm², yielding a correction of $\Delta G_{\text{cyl}} = 5.57$ kJ/mol. Likewise, the PMFs for permeation through the central pore were corrected such that the final PMFs correspond to the density of one central pore per membrane area occupied by one NeRh50 trimer, yielding a correction of 8.30 kJ/mol.

Statistical errors were calculated using bootstrap analysis. From the N umbrella histograms available to compute a PMF, a new equally large set of N histograms was randomly selected (allowing to multiply select a specific histogram). From the new set of N histograms, a PMF was subsequently computed using WHAM. That procedure was repeated 50 times, yielding 50 PMFs and allowing one to compute the standard deviation σ . The error bars in Figures 2, 4, and 5 correspond to 1σ , i.e. to 67% confidence intervals. The 67% confidence intervals at the main barriers for Rh50 and for membranes containing cholesterol or POPG were ~ 2 kJ/mol, and ~ 1 kJ/mol at the main barriers for all other lipid membranes.

The NH_4^+ PMF along the NeRh50 pore was derived from an 100 ns equilibrium simulation of the NeRh50 system containing 150 mM ammonium chloride. The PMF was computed by counting occupancies of NH_4^+ inside a cylinder (radius 3.49 nm) whose axis was aligned along the NeRh50 trimeric axis.

We have carried out NeRh50 simulations with each monomer containing one CO_2 molecule starting at the CO_2 position in the 3B9Z structure published by Li et al.¹⁵ After placing the three CO_2 at the respective positions, the z -coordinates of the three CO_2 molecules were restrained and the system was simulated for 10 ns, allowing the protein to relax with respect to the inserted CO_2 molecules. Subsequently, the simulation snapshots of that simulation after 5, 6, 7, 8, 9, and 10 ns were used as starting structures for 6 independent 40 ns simulations in which the CO_2 was free to diffuse across the channel. With three NeRh50 monomers in each simulation system, these simulations yield 18 independent CO_2 trajectories.

Computation of Membrane Permeabilities. The membrane permeabilities for CO_2 and NH_3 were estimated from simulations in which CO_2 and NH_3 were allowed to diffuse freely across the lipid membranes. Such simulations are referred to as “diffusion simulations” in the following. The membrane permeability P_s for solute s is defined from⁸⁰

$$P_s = \Phi / (A \cdot \Delta C) \quad (2)$$

where Φ denotes the net solute flux in response to the concentration gradient ΔC across the membrane, and A is the membrane cross section area. For the present study, the membrane permeabilities were derived from equilibrium simulations. Accordingly, the bulk solute concentration C_b in the two water compartments (beneath and above the membrane) equaled, and the solutes crossed the membrane in both possible directions (positive and negative z -direction). Assuming that permeation events in opposite directions are independent, that setup is equivalent to a superposition of a solute gradient $\Delta C^{(+)} = C_b$ in positive z direction with a solute gradient $\Delta C^{(-)} = -C_b$ in negative z direction. Hence, by counting permeation events under equilibrium the expected flux in response to a concentration gradient can be computed. To improve the statistics we have counted semipermeation events (i.e., over one membrane leaflet) instead of full permeation events. If n_p denotes the number of semipermeation events in time t (over any leaflet in any direction), the permeability of the full membrane can be computed via $P_s = n_p / (8C_b A t)$. Here, a factor 1/4 is based on the fact that, for one productive full permeation event, four semipermeation events occur on average; that is the solute crossing both leaflets ($n_p = 2$) and, equally often, the solute crossing one leaflet and returning over the same leaflet ($n_p = 2$). The additional factor of 1/2 corrects for the permeation events counted in both directions

(77) Smart, O. S.; Neduvelil, J. G.; Wang, X.; Wallace, B. A.; Sansom, M. S. P. *J. Mol. Graphics* **1996**, *14*, 354–360.

(78) Kumar, S.; Bouzida, D.; Swendsen, R. H.; Kollman, P. A.; Rosenberg, J. M. *J. Comput. Chem.* **1992**, *13*, 1011–1021.

(79) Allen, T. W.; Andersen, O. S.; Roux, B. *Biophys. Chem.* **2006**, *124*, 251–267.

(80) Finkelstein, A. *Water movement through lipid bilayers, pores, and plasma membranes.*; Wiley & Sons: 1987.

during the simulation, whereas the P_s is defined from the flux in one direction in response to a concentration gradient.

Estimation of NeRh50 Single-Channel Permeabilities. Likewise, single-channel permeabilities p_s of NeRh50 for CO₂ and NH₃ were estimated from simulation in which CO₂ or NH₃ molecules were allowed to diffuse freely across the NeRh50 pore. Six independent simulations of 40 ns were carried out for both CO₂ and NH₃ permeating across NeRh50. Starting configurations were created by placing solutes into simulation snapshots randomly taken from the 1.5 ns NeRh50 equilibrium simulation. Twenty-eight solute molecules per NeRh50 monomer were placed into the bulk water and close to the channel axis. To enhance the probability for a solute to enter the pore, the solute molecules were restrained into cylinders of radius of approximately 6.5 Å which were centered along the respective monomeric channel axis. In z -direction the solute molecules were free to diffuse.

The single-channel permeabilities were estimated via $p_s = n/(2tC_b^{\text{eff}})$, where n denotes the number of permeation events, t the simulation time, and C_b^{eff} an assumed effective solute concentration in the bulk. Due to the high solute concentration, the solutes are not independent and may block each other from passing through the pore. For the estimation of p_s we therefore assumed only five independent solutes to contribute to C_b^{eff} and report only the order of magnitude of p_s . To enhance the statistics, also partial permeation events were partially counted if the solute had crossed the main barrier.

To assess if the permeabilities derived from diffusion simulations (across lipid membranes or across NeRh50) are consistent with the respective barriers in the PMFs, we assumed the permeabilities P_s for a solute s to be proportional to $P_s \propto D_s \exp(-\Delta G_{\text{max}}/k_B T)$ (eq 1). The diffusion constants D_s for CO₂ and NH₃ under simulation conditions were computed from the slope of the mean-square displacement of a single solute in a box of pure water, yielding 4.1

$\times 10^{-5}$ cm²/s and 2.7×10^{-5} cm²/s for NH₃ and CO₂, respectively. The proportionality constant between P_s and the right-hand side of eq 1 is not required for the present analysis because the relation is only applied to estimate relative differences in P_s due to differences in the main barrier ΔG_{max} . For instance, given the channel and lipid bilayer barriers $\Delta G_{\text{max}}^{\text{Rh}}$ and $\Delta G_{\text{max}}^{\text{lip}}$, respectively, and the membrane permeability P^{lip} , eq 1 allows one to estimate the permeability of a densely packed Rh50 channels (corresponding to a 2D crystal) to $P^{\text{Rh, 2D}} = P^{\text{lip}} \exp[-(\Delta G_{\text{max}}^{\text{Rh}} - \Delta G_{\text{max}}^{\text{lip}})/k_B T]$. Given a lower expression density of N channel copies per membrane area A , that value translates into $P^{\text{Rh}} = P^{\text{Rh, 2D}} A_{\text{mono}} N/A$ as the contribution of the channels to the overall permeability of the membrane. Note that the above relations hold because we normalize $\Delta G_{\text{max}}^{\text{Rh}}$ such that it corresponds to a channel density of one channel per membrane area A_{mono} occupied by one monomer.

Acknowledgment. This study was supported by the Max-Planck-Society, by a Marie Curie Intra European Fellowship within the 7th European Community Framework Programme, and by the Deutsche Forschungsgemeinschaft (SFB:803).

Supporting Information Available: Figures S1–S4 show trajectories of CO₂ and NH₃ spontaneously permeating across the Rh50 channel and lipid membranes. Figure S5 presents three ammonia PMFs computed for the three individual Rh50 monomers, as well as ammonia/water PMFs for different protonation states of the central twin histidines in the Rh50 pore. This material is available free of charge via the Internet at <http://pubs.acs.org>.

JA102133X